ADVANCED FUNCTIONAL MATERIALS
www.afm-journal.de

A Proof-of-Principle Demonstration: Exploring the Effect of Anode Layer Microstructure on the Alkaline Oxygen Evolution Reaction

*Adarsh Jain, Christian Marcks, Lars Grebener, Jacob Johny, Ahammed Suhail Odungat, Mohit Chatwani, Mena-Alexander Kräenbring, Abhishek Shaji, Marc Frederic Tesch, Anna K. Mechler, Vineetha Vinayakumar, and Doris Segets**

This study explores the effect of nickel cobalt oxide (Ni-Co-O) anode layer microstructure on the oxygen evolution reaction (OER). Four anodes with similar Ni-Co-O loadings and chemical characteristics but distinct morphologies are fabricated by ultrasonic spraying catalyst inks of varying solvent composition (pure water versus a water-ethanol mixture) and drying temperatures (50 and 150 °C) on nickel (Ni) plates. Upon varying solvent composition, particles in the water-based ink exhibited lower stability than particles in the water-ethanol-based ink, boosting the particle connectivity in the layers. This particle connectivity correlated with the mechanical strength of the layers, resulting in reduced contact resistance and enhanced activity. The second observation is that at 50 °C, the surface morphology exhibited hill-like islands with higher roughness, while at 150 °C, concave hemispherical shapes with lower roughness are observed. From 2D-distribution data, it is found that surface roughness correlated with the wettability with electrolyte. Roughness increased the lyophobicity and enhanced the activity through more accessible active sites and efficient bubble transport. This work highlights how microstructure affects macroscopic layer properties, and how these in turn can enhance or diminish the performance of the OER compared to bare Ni, offering insights into the knowledge-based design of anode layers.

1. Introduction

The OER in alkaline water electrolysis (AWE) involves a three-phase contact line,[1] where the electrolyte in the liquid phase serves as a reactant, oxygen produced exists in the gas phase, and the solid phase comprises the catalyst coated-anodes, i.e., anode layers. This contact line is governed by complex flow and transport dynamics, including the drainage of oxygen, paths for electron transportation and the invasion of reactants.[2] Nano-powdered catalysts have attracted significant interest in anode layer fabrication due to their remarkable ability to form specific structures or morphologies.[3] In particular, the precise, stable, and controllable assembly of nanoparticles on anode supports is crucial for achieving electrocatalytic functionality at the three-phase contact line.[4] Despite the importance of layer microstructure in solid-phase applications, their systematic design and targeted modification remain largely

A. Jain, L. Grebener, A. S. Odungat, M. Chatwani, M.-A. Kräenbring, A. Shaji, V. Vinayakumar, D. Segets
Institute for Energy and Materials Processes – Particle Science and Technology (EMPI-PST)
University of Duisburg-Essen
Carl-Benz-Straße 199, 47057 Duisburg, Germany
E-mail: doris.segets@uni-due.de

The ORCID identification number(s) for the author(s) of this article can be found under https://doi.org/10.1002/adfm.202421352

DOI: 10.1002/adfm.202421352

C. Marcks, A. K. Mechler
Electrochemical Reaction Engineering
RWTH Aachen University
Forckenbeckstraße 51, 52074 Aachen, Germany

J. Johny, M. F. Tesch
Heterogeneous Reactions
Max Planck Institute for Chemical Energy Conversion
Stiftstr 34–36, 45470 Mülheim an der Ruhr, Germany

V. Vinayakumar, D. Segets
Center for Nanointegration Duisburg-Essen (CENIDE)
University of Duisburg-Essen
Carl-Benz-Straße 199, 47057 Duisburg, Germany

underexplored. Fabrication process conditions critically define the finally obtained microstructural features including surface roughness, particle distribution, particle connectivity, porosity, pore size distribution, pore connectivity and tortuosity. However, the precise relationships and mechanisms underlying these effects are not well-defined. Moreover, it is still unclear how these microstructures can be translated into macroscopic layer properties like wettability and mechanical stability, and how these macroscopic layer properties ultimately affect the OER. We believe that bridging these knowledge gaps, from microstructure to layer properties and from layer properties to electrochemical performance is essential, in particular during scale-up, for the rational design of advanced alkaline anodes with enhanced OER efficiency.

For tuning the microstructure of layered nanoarchitectures, nanoparticles and their assemblies typically serve as the fundamental building blocks. While nanoparticles are often generated by sol-gel, co-precipitation, hydrothermal and solvothermal synthesis, thermal decomposition and spray pyrolysis up to the industrial scale,[5] their directed assembly in nanostructured layers is an ongoing challenge. Recent studies have explored various methods to design and configure microstructure from the assembly of nanoparticles.[6] On laboratory scale, thermodynamically driven self-assembly utilizes natural interparticle forces such as van der Waals forces, electrostatic interactions, and hydrogen bonding, enabling the spontaneous organization of nanoparticles into ordered structures.[7] This method leverages the inherent properties of the particles and their environment to achieve a desired nanoarchitecture microstructure without external intervention. In contrast, indirect assembly employs the involvement of external forces such as electric or magnetic field-directed assemblies, fluid flow-induced assemblies, or evaporation-induced assemblies and these have been utilized for scale-up.[8] Many indirect techniques and processes adapted from traditional technologies exist in painting, printing, and metal decoration. For instance, electroplating, spray coating, and ink-jet printing offer viable options for applying a thin layer onto the intended supports.[9]

For anode formation in AWE, the indirect assembly of nanoparticles is – among other technologies[10] – applied for the deposition of catalyst particles onto support materials such as plates, meshes and foams, ensuring proper adhesion and functionality.[11] However, despite many researchers utilized these techniques to fabricate anode layers for water splitting, the correlation between microstructure, anode layer wetting, mechanical strength and electrochemical performance is still concealed.

In this study, we adjusted the microstructure of four anode layers by applying two different solvent compositions commonly utilized for transition metal oxide-based inks during ink formulation,[12] pure water and a mixture of water and ethanol. These were applied at two different drying temperatures, 50 and 150 °C, during ultrasonic spray coating. We demonstrated how catalyst stability correlates with the solvent composition using transmittogram and S-score analyses from stability trajectories developed by us.[13] The fabricated microstructure of the anode layers was characterized and quantified by top view scanning auger electron microscopy (SAM), topographical atomic force microscopy (AFM), and cross-sectional focused ion beam scanning electron microscopy (FIB-SEM). Subsequently, we analyzed the correlation between the microstructure and the two key anode layer properties: wetting and mechanical strength of the layers. Upon having access to these usually unknown properties, ultimately, we were able to correlate the microstructure of the generated anodes with their wetting and mechanical strength, and to further connect these properties with beaker cell electrochemical activity and stability data. Taken together, our approach enables to decipher the process-microstructure-property-performance relationships that are crucial to enhance electrochemical processes and mechanisms.[14]

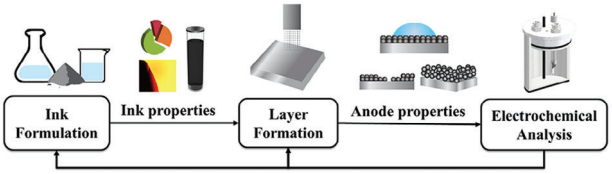

Figure 1. Schematic representation of the developed strategy for the fabrication, microstructure and property assessment of anode layers, including ink formulation, layer formation by coating, microstructure assessment and electrochemical analysis.

2. Results and Discussion

2.1. Strategy for the Rational Design of Anode Layers with Electrochemical Assessment

First, a strategy was developed that enables to correlate microstructure with electrochemical performance. The challenge was to fabricate anode layers that vary in the decisive properties such as surface roughness, wetting behavior, and mechanical strength, while maintaining comparable mass loading and constant chemical composition. The fabrication strategy is delineated in **Figure 1**. It illustrates the progression from the selection of the necessary components to electrochemical performance testing and can be divided into three main stages: an ink formulation stage, a layer formation stage and an electrochemical analysis stage. Each stage presents specific challenges, and advancing through the entire process chain is labor-intensive, yet essential for elucidating the underlying process-microstructure-property-performance relationships.[14,15]

In brief, we focused on two key factors: solvent composition and drying temperature. Based on initial observations, we hypothesized that these factors significantly affect anode layer properties and ultimately, electrochemical performance. Preliminary tests were conducted to fine-tune the factor levels and ensure experimental reproducibility for investigating wetting and mechanical properties. This groundwork allowed us to employ systematic experimental design.

In the initial stage, to investigate the impact of the first factor, the carrier liquid, on the structure and property of the layers, we prepared two catalyst inks: one with water and the other with a 1:1 mixture of water and ethanol, utilizing Ni-Co-O as the catalyst and Nafion as the binder.[16] Subsequently, we examined the dispersibility and stability of the prepared inks.

In the second stage, the analyzed inks were deposited on a Ni plate, i.e., the anode support, by ultrasonic spray coating. To unravel the effect of flow- and evaporation-induced nanoparticle-assembly on the anode support, we set two distinct heating temperatures (second factor): 50 °C, which is a considerable temperature to evaporate inks near to atmospheric conditions and 150 °C, which is larger than the boiling points of the utilized carrier liquids. At this point, it should be noted that the glass transition temperature of Nafion occurs at ≈130 °C.[17] At temperatures slightly above this point, the polymer transitions from a glassy to a rubbery or viscous state, which is further influenced by the swelling of Nafion in the presence of alcohol.[18] However, after the drying process, Nafion is expected to regain its original chemical composition, as it maintains chemical stability up to 280 °C.[19] In this work, we introduced Nafion – though being designed for proton, not for hydroxyl ion transport – to enhance the mechanical stability of the layers. In the following, we refer to the water-based ink applied at 50 °C as W-50C and at 150 °C as W-150C. Similarly, the ink made with the water-ethanol mixture as continuous phase applied at 50 °C is denoted as WE-50C, and at 150 °C as WE-150C.

Subsequently, we analyzed the microstructure of the four resulting anodes and related them with macroscopic layer properties like the initial wetting with the electrolyte (lyophilicity/lyophobicity) and mechanical stability.

In the last stage, we utilized a beaker cell setup to evaluate the electrochemical activity and stability of the four anodes, W-50C, W-150C, WE-50C and WE-150C.

This methodology enabled us to discern the significance of solvents and drying temperatures on layer properties and, ultimately, on electrochemical performance. The detailed experimental setups and parameters are described in the Experimental section.

2.2. Microstructure Formation and Assessment

2.2.1. Catalyst Ink Properties

Figure 2 illustrates the sedimentation of catalyst nanopowders in water and water-ethanol with Nafion binder. The ink dispersions were analyzed using transmittograms, which in brief enable the direct visualization of the transmittance along the radial position of the measurement cell over the sedimentation time (Figure 2a,b) and can be further evaluated through S-scores as stability-metric, both recently developed by us (Figure 2c).[13] By analyzing the characteristic patterns during the sedimentation process, the initial dispersion state, formulation stability against agglomeration, interaction of catalyst materials, and lifespan of the inks can be assessed.

The transmittograms in Figure 2a,b show a distinct difference in the sedimentation behavior between the two formulations. For pure water (Figure 2a), the sedimentation is relatively rapid, with high transmission levels observed early on and minimal gradient formation, indicating fast settling of particles. In contrast, using the water-ethanol mixture as continuous phase (Figure 2b) results in a slower sedimentation process, with a more gradual transmission gradient over time, suggesting a slower settling rate. This difference is quantitatively analyzed by the stability trajectory shown in Figure 2c. The S-score for water shows a sharp maximum at 4.4 min, where the bulk sedimentation occurs, which represents the maximum of particles that are sedimented at this point, indicating rapid sedimentation. The complete sedimentation of the particles occurred ≈20 min at the

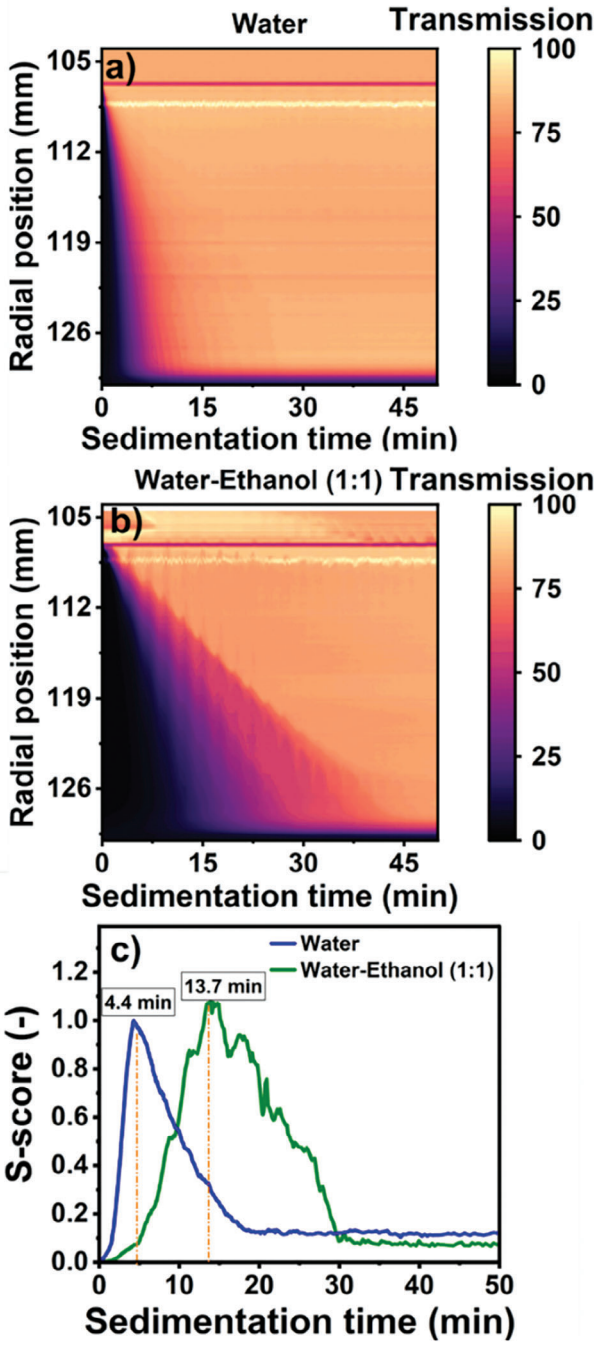

Figure 2. Visualization of the time-resolved sedimentation process via transmittograms: a) Ink prepared using pure water as a solvent, b) ink prepared using a mixture of water and ethanol as continuous phase (1:1 ratio) and c) direct comparison of both inks via stability trajectories. Two measurements were conducted (sample size, $n = 2$) and the resulting mean ± standard deviation (SD) is tabulated in **Table 1**.

Table 1. Key physical properties: Viscosity (η), density (ρ) of carrier liquid, and relative sedimentation time at bulk sedimentation (RST_{BST}) of the inks. Data was measured at 293 K.[21]

Carrier liquids	$\eta \times 10^{-3}$ [Pa·s]	$\rho \times 10^{3}$ [kg m^{-3}]	$RST_{BST} \times 10^{15}$ [m^{-2}]
Water	1.01	0.99	5.34 ± 0.16
Water-Ethanol	2.37	0.85	7.95 ± 0.21

relative centrifugal acceleration (RCA) of 733.7, which is equivalent to 10 days and 11 h in real-time stationary conditions (RCA = 1). For the water-ethanol mixture, the sedimentation process is more prolonged, with the S-score reaching its bulk sedimentation at 13.7 min. The sedimentation of all particles occurred approximately after 30 min, which is equivalent to 15 days and 6 h at RCA = 1. Noteworthily, the addition of Nafion as a binder did not affect the sedimentation behavior and thus the stability of the ink formulations, as highlighted by the S-score before and after its addition in Figure S1b (Supporting Information). Although this result was unexpected, it can be explained by the lack of specific affinity of Nafion to the particle surface, indicating no significant chemisorption and likely no pronounced physisorption. This suggests that the stability of the inks is predominantly governed by the solvent composition rather than the presence of Nafion. The effect of key properties of the continuous phase, such as viscosity and density can be evaluated in combination as defined by Süß et al.[20] This is accomplished by determining the relative sedimentation time (RST) at bulk sedimentation. Determined RST_{BST} along with carrier liquids properties are shown in Table 1. The pure water-based ink has an RST_{BST} of 5.34×10^{15} m^{-2} and the water-ethanol-based ink has a significantly higher value of 7.95×10^{15} m^{-2}. At constant catalyst particle size, the higher the RST_{BST}, the higher the stability of the formulation over time and the longer the shelf-life.

The differences in RST_{BST} values can be explained by the interplay between viscosity and density of the carrier liquids. Viscosity directly influences the sedimentation behavior by increasing the drag force acting on suspended particles.[13] Higher viscosity slows the sedimentation rate, resulting in enhanced stability. In this study, the water-ethanol mixture has a significantly higher viscosity ($\eta = 2.37 \times 10^{-3}$ Pa s) compared to pure water ($\eta = 1.01 \times 10^{-3}$ Pa s), contributing to its higher RST_{BST} value. On the other hand, density affects the buoyant force acting on particles. Although the water-ethanol mixture has a lower density ($\rho = 0.85 \times 10^{3}$ kg m^{-3}) compared to pure water ($\rho = 0.99 \times 10^{3}$ kg m^{-3}), the increased viscosity dominates, leading to greater suspension stability for the water-ethanol ink.

Taking together, the change in ink characteristics is mainly attributed to the different interactions of the particles with the carrier liquids used as continuous phase causing faster agglomeration in pure water and enhanced stability in water-ethanol mixtures. The overall results highlight the significant impact of solvent composition and the interplay between solvents on sedimentation behavior, leading to a change in stability of the catalyst inks.

Next, the analyzed inks were deposited on Ni plates for fabricating layers with different morphology. Given the high level of automation provided by the ultrasonic spray coating equipment employed in this study, all parameters, except the herein targeted solvent composition in the ink formulation and the drying temperature, could be kept constant (details are summarized in the Experimental section). In the following, the assessed microstructure of all four anodes will be discussed in detail.

2.2.2. Chemical Properties of Anode Layers

Investigating potential chemical changes during processing necessitated the employment of a wide range of analytical techniques, including Raman spectroscopy, energy-dispersive X-ray spectroscopy (EDX), Fourier-transform infrared spectroscopy (FTIR), X-ray photoelectron spectroscopy (XPS) and X-ray diffraction (XRD). The results obtained from each technique are discussed and summarized in section S2 (Supporting Information). By comparing results obtained from different complementary techniques (Raman, EDX, FTIR, XPS and XRD), it can be concluded that the chemical nature of the as-obtained anodes including the chemical signature of the binder molecules, remains constant within the detection limits of the analytical devices across the varied processing parameters. Neither the drying temperature nor the solvent matrix utilized as continuous phase in the ink formulation showed a significant chemical impact. We ascribe this to the fact that the drying process was operated clearly below 280 °C, such that Nafion is expected to remain thermally stable. This absence of any change in the chemical properties is critical for comparing the different layers obtained here in terms of their microstructure and connecting microstructural changes with macroscopic layer and electrochemical properties.

2.2.3. Microstructure of the Four Anode Layers

Microstructure analyses in terms of the underlying surface morphology of the layers were performed utilizing top view SAM, topographical AFM, and cross-sectional FIB-SEM. The results gained at high magnification above 1000x are depicted in **Figure 3**. Noteworthily, morphological analysis at low magnification, 100x (not shown) revealed that there is no evidence of cracks due to improper coating or drying on the surfaces. Already a first qualitative assessment of the gathered data revealed distinct surface morphologies between layers fabricated at lower temperatures (Figure 3a,c) and those produced at higher temperatures (Figure 3b,d). Layers formulated with water-ethanol-based ink exhibited more defined and structured surface features compared to those prepared with water-based inks.

Additionally, AFM characterization further revealed that at the lower drying temperature (50 °C), the anode surfaces displayed hill-like islands that are identifiable by the red color. These islands are ascribed to distinct assemblages that are formed during coating and drying (Figure 3e,g). Conversely, at higher temperature (150 °C), the surfaces exhibited reduced island formation that is seen by the larger share of purple and blue regions (Figure 3f,h). Moreover, an ordered pattern with distinct motifs arises at a higher temperature, which becomes particularly evident in case of WE-150C (Figure 3d). Closer analysis at higher resolution (insets of Figure 3b and especially of Figure 3d) indicates that the surface morphology transitions to a concave, hemispherical shape. This shape resembles structures commonly seen in

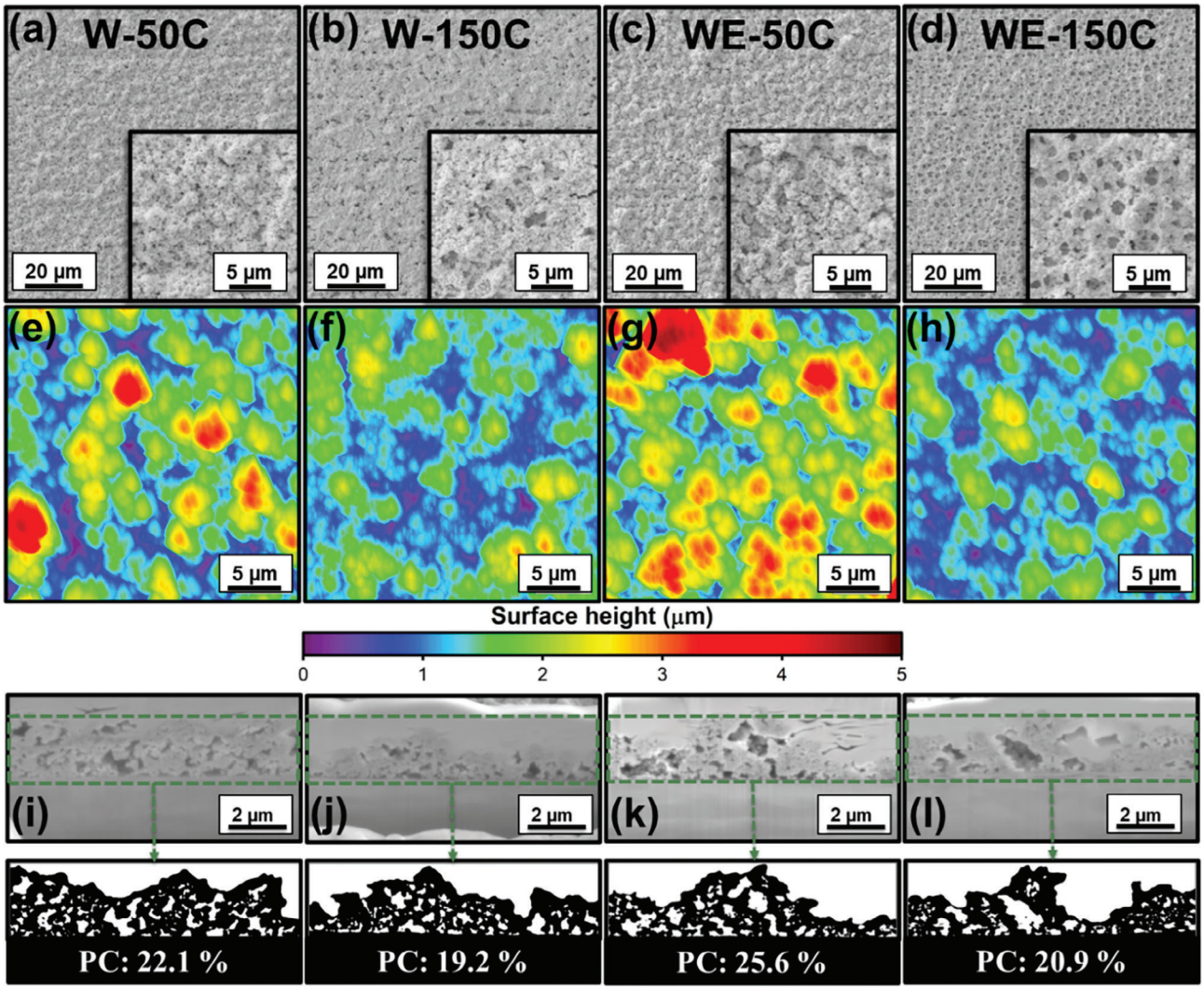

Figure 3. Morphology analysis using SAM: a) W-50C, b) W-150C, c) WE-50C, d) WE-150C. Morphology analysis using AFM: e) W-50C, f) W-150C, g) WE-50C, h) WE-150C. Cross-sectional analysis of anodes obtained using FIB-SEM along with binarized images of anodes and PC: i) W-50C, j) W-150C, k) WE-50C, l) WE-150C.

nature, such as the nest of a bird or a shallow pot. These are characterized by a curved inward surface that encloses a space, which provides an intuitive visualization of the observed concave morphology. These observations are in line with cross-sectional imaging data (Figure 3i–l) that provided further insight into the depth profile of the fabricated anodes.

However, since distinguishing the morphologies visually was challenging and inevitably remains subjective and in parts speculative, we applied image analysis (details are summarized in the Experimental section) to quantify the differences. Specifically, the pore coverage (PC) was utilized to further compare the fabricated anodes. In brief, PC is defined as the cross-sectional area covered by pores compared to the cross-sectional area covered by catalyst material. The determined PC values for the layers are as follows: W-50C is 22.1%, W-150C is 19.2%, WE-50C is 25.6%, and WE-150C is 20.9%. Here it is observed that the PC appears to be slightly higher for the layers fabricated at lower temperatures for both ink formulations.

To further underpin the quantitative analysis of microstructure, we extracted microstructural features such as surface roughness and homogeneity score as described in our previous work along with additionally measured thickness.[22] In brief, multistage data quantification (MSDQ) is a statistical framework that enables the extrapolation of surface features of a complete layer using targeted analyses from a representative amount of local regions (for details, refer to the Section S3, Supporting Information). Here, thickness refers to the measured depth and valleys of the anode layer, surface roughness quantifies the average deviations in height, and the homogeneity score reflects the evenness of the surface across the analyzed area. These features were extracted using AFM to assess thickness, where a portion of the coated layer was removed to establish a baseline reference. These features are illustrated in **Figure 4**. Figure 4a,b shows the variations in peaks and valleys among the four fabricated anodes. W-50C and WE-50C exhibit elevated peaks and deeper valleys compared to W-150C and WE-150C. Figure 4c shows the increased

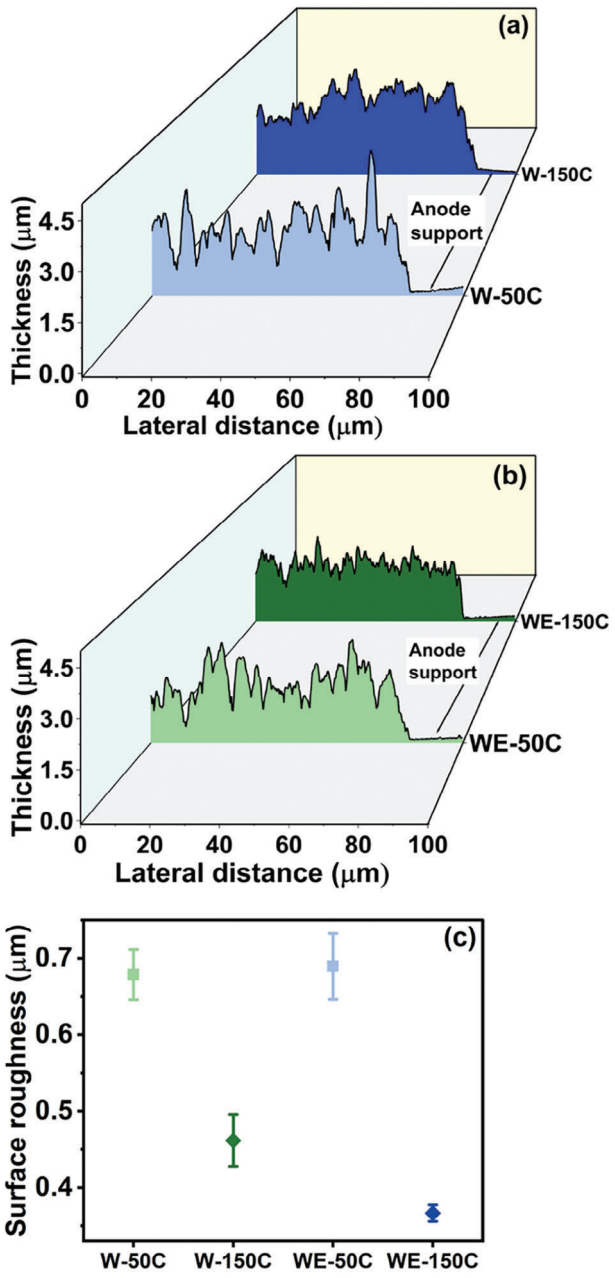

Figure 4. Surface features extraction from AFM data. Thickness of anode layer a) W-50C and W-150C, as well as b) WE-50C and WE-150C. Representative features extraction via MSDQ, statistical details are tabulated in Table S1 (Supporting Information): Root mean square surface roughness c).

surface roughness for the W-50C and WE-50C anodes compared to W-150C and WE-150C. In contrast, the inverse homogeneity score is expectedly larger due to the lower surface variation observed for the W-150C and WE-150C anodes compared to samples W-50C and WE-50C. All measured microstructural features are collectively summarized in **Table 2**.

From the above results, it becomes evident that the drying temperature plays a major role. This can be understood as follows: During the spray coating process, it was observed that at a lower temperature (50 °C), the evaporation is markedly slower. On the contrary, at an elevated temperature (150 °C), ink droplets evaporate almost instantly, often without any visible wetting of the surface as soon as the droplet contacts the anode support.[23] Additionally, it must be noted that when liquids are dropped on a support at temperatures higher than their boiling point, a thin layer of vapor forms that insulates the droplet and prevents it from rapidly boiling away, known as the Leidenfrost effect.[24] Therefore, as the drying temperature significantly affects the rate of evaporation, the spread of ink droplets, the wetting behavior of the ink, and the swelling of the binder, it strongly determines the particle distribution, particle connectivity and formation of particle assemblies on the substrate surface.[25] After the detailed assessment of microstructural features, the question is now how they affect macroscopic anode layer properties. This will be discussed in the next section.

2.3. Macroscopic Properties of Anode Layers

In this section, we extract macroscopic properties such as wetting as the initial interaction with the electrolyte (here: 1 M KOH) during OER and mechanical strength of the generated layers.

2.3.1. Wetting Analysis

Wetting is a vital process that defines the mass transport mechanism during the OER. However, analyzing dynamic wetting is a complex task. In this subsection, we focused on assessing the initial wetting behavior of electrolyte on the surface of the generated layers. The contact angles measured on the four layers are depicted in **Figure 5**a–d. Anodes produced at 50°C (W-50C and WE-50C) exhibited very similar mean contact angles of 149.01 ± 5.18° and 153.05 ± 4.80° respectively, attributing their nearly super-lyophobic (150–180°) nature. In contrast, anodes fabricated at 150 °C (W-150C and WE-150C) showed smaller contact angles of 119.25 ± 1.17° and 123.43 ± 3.32°, indicating a slight reduction in lyophobicity (90–150°) compared to those produced at 50 °C. In this work, we utilize the terms *lyophilic* (0-90°) and *lyophobic* (90–180°) to describe surface-electrolyte interactions, which are comparable to *hydrophilic* and *hydrophobic* interactions when water is the contacting liquid. However, several studies have employed the terms *lyophobic* and *lyophilic* to describe interactions involving other liquids as the contacting medium.[26] Taking the standard deviation into account, the solvent composition used in the ink formulation did not significantly affect the surface wettability. Instead, the primary factor influencing wettability is the temperature used during the coating process.

Contact angles measured from the selected regions were plotted using a 2D density plot (or kernel plot).[27] This visualization helped to understand the relationship between surface roughness and contact angles, and their distribution across the layers. Specifically, Figure 5e,f explores the found relationship between roughness and contact angles, where it is observed that a lower roughness corresponds to a lower contact angle, implying increased wettability on the surface. This trend is consistent in

Table 2. Surface characteristics: Morphological shape, PC, surface roughness (R_s) and homogeneity score (H_s) for W-50C, W-150C, WE-50C and WE-150C.

Features	W-50C	W-150C	WE-50C	WE-150C
Shapes	Hill like Islands	Concave hemisphere	Hill like Islands	Concave hemisphere
PC/%	22.1	19.2	25.6	20.9
R_s/μm	0.62–0.71	0.42–0.50	0.60–0.76	0.35–0.37
H_s/-	0.68–0.73	0.83–0.87	0.67–0.77	0.86–0.88

both kernel plots, and it is important to note that it is the same for both continuous phases applied in the ink formulation. This underscores the role of surface roughness, in addition to the chemical composition, in modulating surface wettability of anodes for AWE.

Our findings align with existing studies that apply the Cassie-Baxter model in surface-liquid interface analysis.[28] In brief, the Cassie-Baxter model describes a scenario where air pockets are trapped under the liquid, leading to the observation of increased contact angles in heterogeneous systems.

$$Cos\theta\ [CB] = f_s\left(1 + \cos\ \theta\left[flat\right]\right) - 1 \quad (1)$$

where θ[CB] is the measured contact angle on the rough surface, f_s is solid/liquid contact area, θ[flat] is the contact angle of the flat surface with similar intrinsic material properties.

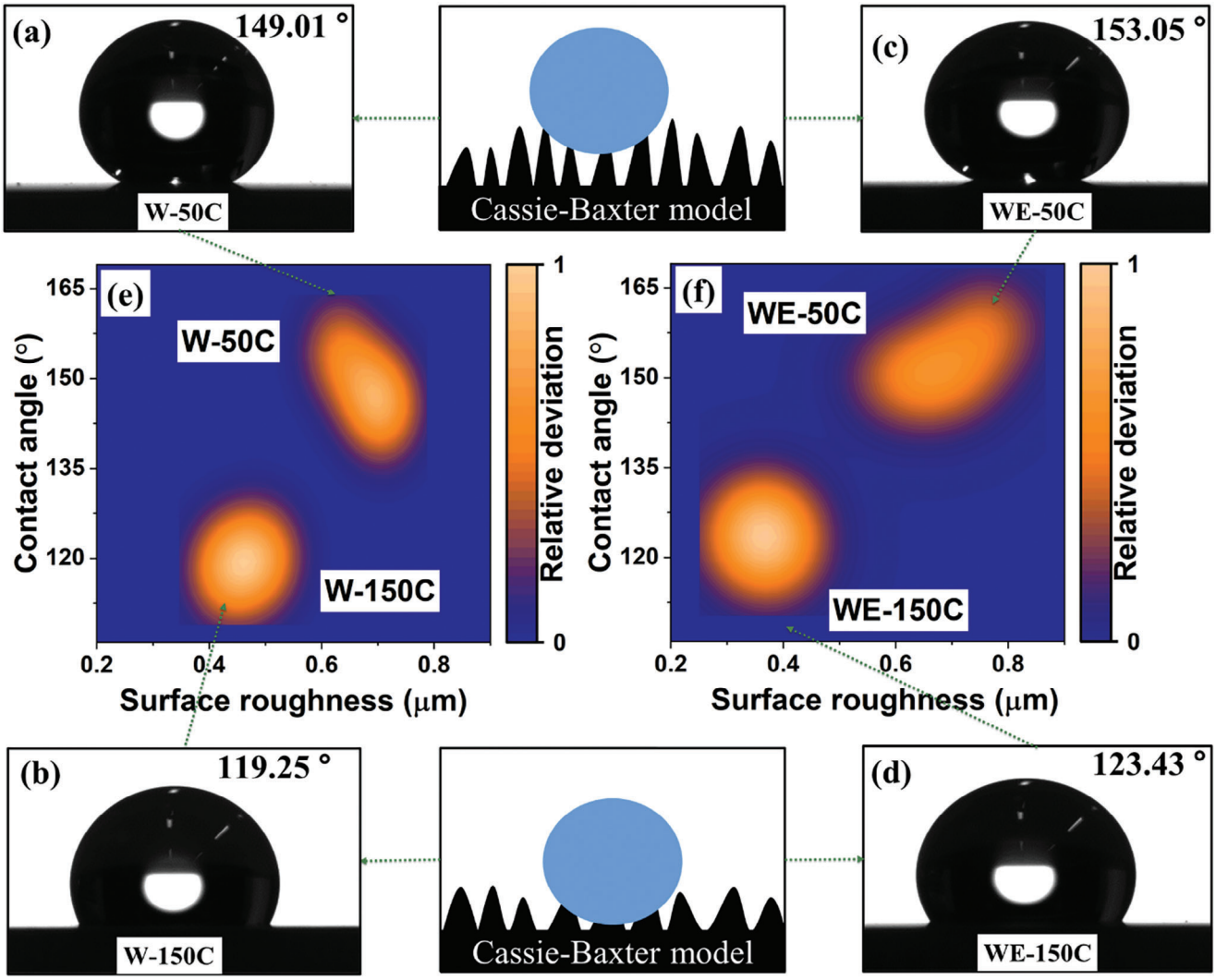

Figure 5. Static contact angle on spray-coated anodes along with wetting models: a) W-50C, b) W-150C, c) WE-50C, d) WE-150C. Relation between the surface roughness and contact angle of the layers: e) surface roughness versus contact angle for water-based anodes, f) surface roughness versus contact angle for water-ethanol-based anodes. Three measurements were conducted (n = 3) and the resulting mean ± SD is found in **Table 3**.

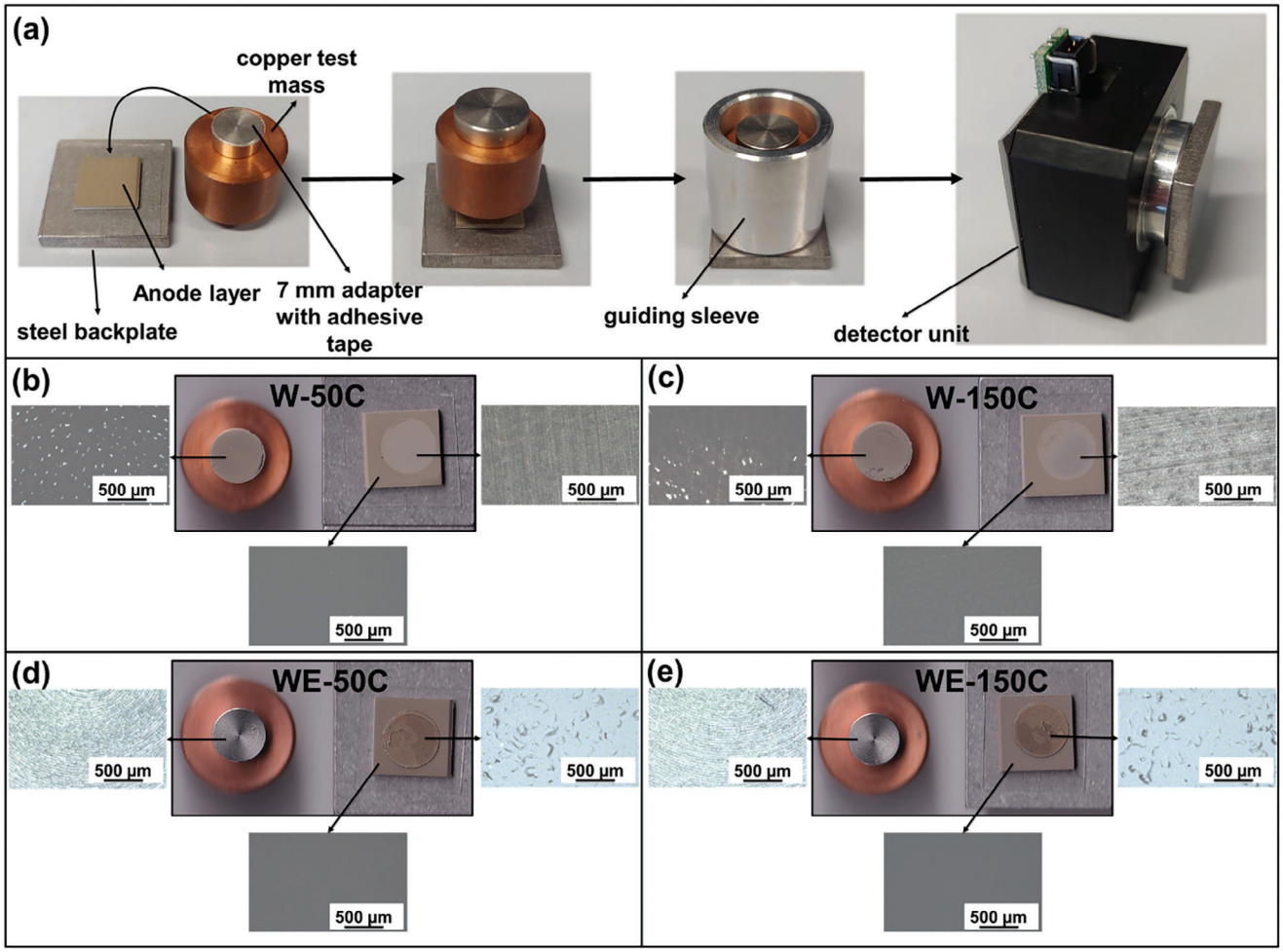

Figure 6. Adhesion analysis by centrifugal detachment. Assembly of specimens for adhesion analysis a) with images after centrifugal detachment along with micrographs of adapter (left), layer (below), and after rapture (right): b) W-50C, c) W-150C, d) WE-50C, e) WE-150C. Three measurements were conducted (n = 3) and the resulting mean ± SD is reported in Table 3.

In our system, we found that the PC is an effective qualitative indicator for predicting the wetting state, that could be even used quantitatively when the contact angle of the smooth surface would be known. We ascribe this to the fact that the PC of the layers defines the amount of air trapped within the anode microstructure in such a way that higher PC results in more air entrapment. In conclusion, the found trend in roughness and PC aligns with the expected behavior when assuming the wetting behavior to follow the Cassie-Baxter model. Though not yet being frequently used in the community of water electrolysis and just described in a few studies, mostly driven by researchers focusing on porous media,[29] we believe that the Cassie-Baxter model could enable to understand the mechanisms underlying bubble removal and open a pathway for the rational design of electrode surface morphology.

2.3.2. Adhesion Analysis

A major problem with anode layers in AWE is degradation and delamination over time. Despite these challenges, such sources for failure are rarely measured due to the complexity and tedious nature of the process. In this work, we utilized a commercial device for centrifugal detachment and developed a measurement routine specifically for nanoarchitecture layers to evaluate the mechanical strength (see the experimental section for measurement protocols). In brief, the specimens for adhesion analysis by centrifugal detachment were assembled as shown in **Figure 6a**. The Ni supports with catalyst layers are bonded to a steel backplate. A copper test mass is glued on top of it with a defined adapter area. All together are inserted into a guiding sleeve and a detector. Thus, centrifugal forces can be applied orthogonally to the catalyst layer on the Ni substrate until the detector determines the breaking of the specimen. The fracture images of the fabricated layers, presented in Figure 6b–e, revealed distinct features: the left side of each image shows the adhesive-mounted assembly, while the right side displays the anode glued onto the measurement support. These images were captured post-measurements.

For anodes fabricated with water-based inks, the strengths at cohesive failures are 0.77 ± 0.10 and 0.45 ± 0.09 MPa for W-50C and W-150C, respectively. This indicates the superior interfacial strength between anode support and catalyst layer compared to

the inter-particle strength within the layer. However, some parts of the catalyst particles in the anode layer were detached from the anode support, as is evidenced in micrographs that were taken after fracture-testing and that are shown in Figure 6b,c. Additionally, adapter micrographs in Figure 6b,c present the holes within the layers. From this we conclude a weaker particle connectivity in terms of cohesion within the anode layer than adhesion between the particles and the Ni support. In stark contrast, anodes fabricated with a water-ethanol mixture, depicted in Figure 6d,e, exhibit fractures at the adhesive utilized for the adherence experiments and particles indicating high mechanical strength. In comparison, anodes produced with the WE mixture show strengths of 1.57 ± 0.18 and 1.28 ± 0.23 MPa at adhesive rupture for WE-50C and WE-150C respectively. This demonstrates stronger interparticle connectivity within the anode layer and improved interfacial strength between the anode layer and the anode support.

For instance, taking the standard deviation into account, the drying temperatures showed negligible effect on the mechanical strength of the layers. Instead, the solvent choice in the ink formulation emerged as the dominant factor influencing the mechanical properties. Despite the still ongoing challenge in interfacial characterization of nanoarchitecture layers that prevents us from making quantitative conclusions about microstructural effects on the mechanical strength, it is clear that the interaction between the continuous phase, binder, and coating process mechanisms at different drying temperatures plays a crucial role. This interplay can be explained as follows:

1) First, as noted in section 2.2.1, a stable ink, such as the Ni-Co-O particles dispersed in water-ethanol mixtures, ensures a uniform distribution of particles over the anode support, leading to increased contact area between particles within the layers. In contrast, agglomerates that form in the less-stable water-based ink spread on the support, creating weaker connectivity of particles.
2) Second, as mentioned in Section 2.1, the added Nafion binder can swell in the presence of alcohol,[30] further enhancing the binding strength between particles at their contact points formed during coating and drying.
3) Third, as noted in the previous section, the lyophobic nature of the layers during multilayered coatings plays a significant role. Initially, the water-based coatings spread well on the Ni plate due to its lyophilic properties. However, after several layers are applied, the presence of Nafion renders the surface more lyophobic/hydrophobic, slowing down the wetting of subsequent layers and thereby reducing interparticle cohesion. This effect is minimum in case of water-ethanol based coatings.
4) Lastly, the azeotropic boiling point of the catalyst inks must be also considered as a co-solvent-effect in case of water-ethanol based coatings. Since the utilized mixture of water-ethanol (0.5:0.5) in the respective ink is lower than the azeotropic composition of water-ethanol (4.375: 95.635),[31] ethanol evaporates first, followed by water, which remains in the liquid phase. This process influences the process of layer formation,[32] thus impacting the particle connectivity.

Altogether, the measured difference highlights the prevalence of cohesive failure in anodes utilizing pure water as continuous phase and the stronger mechanical strength observed in water-ethanol-based anodes due to stronger interparticle connectivity.

This analysis of anode layer properties underscores the intricate relationship between the microstructure of the catalyst layer in terms of the PC as well as the surface roughness with wettability and the mechanical properties of the coatings. All layer properties are summarized in Table 3.

The interplay between KOH and the anode surface is important and shall not be overlooked as it governs both the bubble removal and the adsorption of reactants during OER.[33] But also the requirement of mechanical stability is obvious, especially when rationalizing that interparticle connectivity and the interface between anode layer and anode support helps in avoiding contact resistance, and durability of anodes in OER.[34] However, so far only anode layer properties were quantified and hypothetically linked with electrochemical properties. Therefore, in the last chapter, we will close this gap and connect microstructure and the resulting layer properties with electrochemical performance measures.

2.4. Electrochemical Properties of Anode Layers

Electrochemical characterization was carried out using a three-electrode beaker-cell setup, adjusted for plate electrodes from the work presented by Thissen et al.[35] Please see the Experimental section and supplementary information, section S4, for a detailed description of the measurement protocol.

2.4.1. Ionic and Contact Resistance within Beaker Cell

The uncompensated resistance (R_u) refers to the inherent resistance within the electrochemical cell, measured when no current flows. R_u is primarily composed of ionic electrolyte resistance, as well as inter-particle contact resistances between particles and the support. Since the electrolyte and the anode support were identical for all measurements, we attribute the measured differences mainly to the particle-particle and particle-support interactions. **Figure** 7a,b shows the R_u measured before and after OER. Due to the proximity of the reference electrode to the working electrode (see Experimental Section), all R_us are well below 1 Ω. The influence of ink composition on R_u is evident: R_u is lower for WE-50C and WE-150C compared to W-50C and W-150C, both before and after OER measurements. More notable differences in R_u are observed when comparing the different drying temperatures: While between W-50C and WE-50C a difference of ≈150 mΩ is present, the difference between W-150C and WE-150C is only 50 mΩ and for both electrodes the R_u drops slightly after OER.

Particularly in the case of a microstructure with higher surface roughness and PC (W-50C and WE-50C), ionic and contact resistance correlate directly with the adhesion analysis presented in the previous section. Water-based anodes exhibit weaker interparticle cohesion, leading to increased contact resistance. This suggests that the mechanical strength of the anode layers, defined by the inter-particle connectivity, has a direct impact on the R_u. However, in the case of a microstructure with lower surface roughness and PC (W-150C and WE-150C), a slight dependency of the mechanical strength on R_u is observed.

Table 3. Anode layer properties: Measured contact angle (θ) and mechanical strength (σ) for W-50C, W-150C, WE-50C and WE-150C.

Properties	W-50C	W-150C	WE-50C	WE-150C
θ/°	149 ± 5	119 ± 1	153 ± 4	123 ± 3
σ/MPa	0.77 ± 0.10	0.45 ± 0.09	1.57 ± 0.18	1.28 ± 0.23
Wettability	Super-lyophobic	Lyophobic	Super-lyophobic	Lyophobic
Mechanical failures	Cohesive	Cohesive	No failure	No failure

2.4.2. Electrochemical Activation by Conditioning

Electrochemical conditioning is commonly applied to remove contaminants from the electrode surface and ensure reproducible starting conditions for every sample. Furthermore, it can also activate the electrode and improve its performance.[36] Here, we give a qualitative description of the process-induced surface changes by analyzing the conditioning cycles of the different electrodes. **Figure** 8a,b shows the 5th (dashed lines) and 50th (solid lines) cycles of the conditioning step. All anodes increase the surface charge passed for every cycle throughout the procedure. This is ascribed to the growth of the hydroxide layer during the phase transition from $Ni(OH)_2$ to NiOOH species at higher potentials on the catalyst surface, which essentially forms a NiOOH/CoOOH-like structure.[37] When comparing the 50 °C anodes with the 150 °C anodes as well as the W and WE based inks, a distinct difference is observed for the charge passed during the redox transitions. In general, the WE-based electrodes show larger redox-charges than those prepared with pure water. Furthermore, the electrodes dried at 50 °C both show larger redox features than their 150 °C counterparts. Overall, the charge over the oxidation/reduction peak after conditioning arrange in the order, WE-50C>W-50C≥WE-150C>W-150C. For all samples, we observe two (distinct) redox features. While the intensities vary, the peak positions of all anodes are similar. This indicates no differences in the present Ni-Co-O-phase, which is in line with the microstructural analysis presented in section 2.2. At this point it needs to be mentioned that from the conducted Raman spectroscopy, the active OER species within Ni-Co-O layers cannot be effectively analyzed using the conducted ex-situ Raman measurements, as these phases are expected to form only under operando conditions, such as constant applied potentials or potential cycling.[36] For instance, Chen et al.[38] identified a NiOOH-h-CoO_2 active structure in Ni-modified CoO_xH_y films during OER using *operando* Raman spectroscopy, linking it to enhanced catalytic activity. Thus, implementing *operando* Raman measurements on Ni-Co-O layers in future studies could provide valuable insights into the identification and comparison of OER active species in these catalysts.[39]

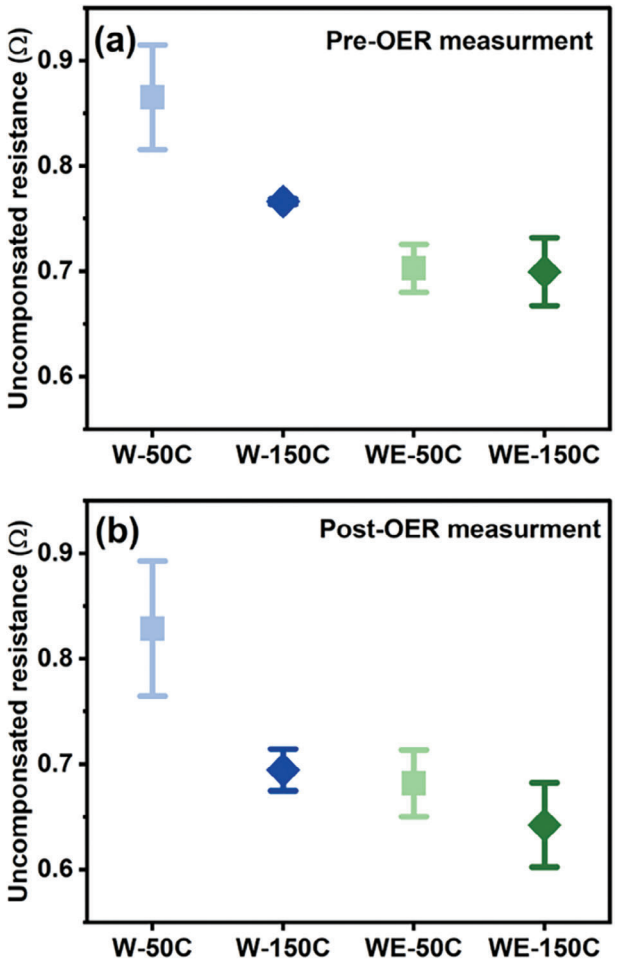

Figure 7. R_u between electrolyte, anode layer and support, measured at open circuit potential at different points of the protocol. a) Pre-OER measurement, b) post-OER measurement. Three measurements were conducted (n = 3), and the results are represented as mean values with error bars indicating SD.

The change in passed surface charge is a qualitative indicator that the surface area for hydroxide formation has increased, or that the -OOH formation is facilitated, yielding more of the suspected OER-active γ- or β-NiOOH-phase. However, a quantitative analysis of the electrochemical active surface area is not attempted due to the mixed-metal species in Ni-Co-O, making the assignment of the charge to individual active sites impossible.

2.4.3. Electrochemical Activity

The activity and stability of anode layers are critical factors in determining the overall efficiency and durability of electrochemical systems, particularly in reactions like the OER. **Figure** 9a illustrates the behavior of the electrodes during the 2 h chronopotentiometry (CP) of the last protocol cycle as well as that of a bare Ni-support (Ni99.2). Ni itself exhibits a distinct non-porous microstructure and demonstrates excellent OER performance when exposed to iron-containing electrolytes.[40] Here, electrolytes with

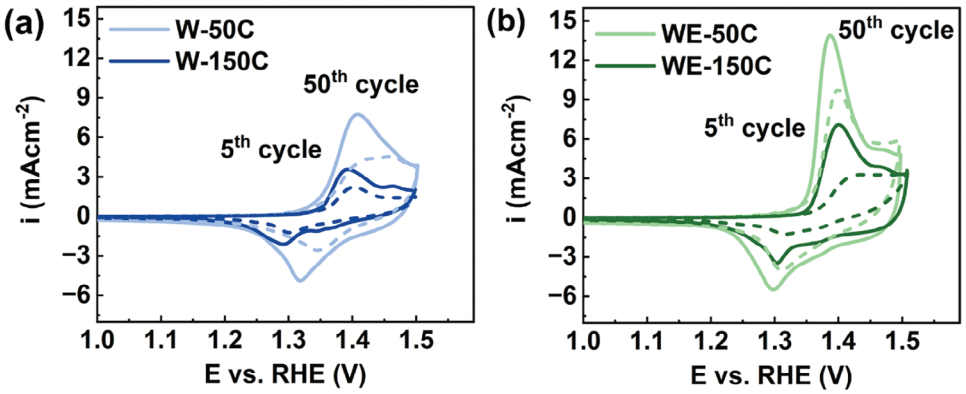

Figure 8. a) Conditioning of W-50C and W-150C and b) conditioning of WE-50C and WE-150C. Three measurements were conducted (n = 3) for each anode, here a representative dataset was selected to illustrate the differences. Data on the two other measurements can be extracted from the Section S5 (supporting Information).

a constant Fe-content of 200 ppb were used and Ni is used primarily as a reference point for comparison. In total, four CPs were conducted, the corresponding graph can be found in Section S5 (Supporting Information). Please note that the peculiar activation and deactivation behavior of the anodes in between protocol cycles is the objective of ongoing investigations. All coated electrodes show a slight activation, as the potential drops over the 2 h experiment. While W-150C and WE-150C have a higher potential at the beginning of the CP, they almost converge with the bare Ni-support towards the end. Interestingly, despite maintaining constant mass loading (415 ± 30 µg cm^{-2}) and similar chemical compositions (see section 2.2.2), W-50C and WE-50C exhibited superior performance relative to the Ni-support (Ni99.2), with a lower potential of ≈40 mV at the end of the CP for WE-50C.

The dynamic activity measurement by cyclic voltammetry (CV) (Figure 8b) further corroborates the distinct performance differences in the anodes. The CVs reflect the activities as recorded at the beginning of the CP, though they were measured at the end of the protocol. At 100 mA cm^{-2} the potentials range from 1.578 to 1.642 V, and the activities are arranged in the order WE-50C>W-50C>Ni-support>WE-150C>W-150C. As described in section 2.4.2, this performance difference aligns well with the passed charge. This trend clearly shows that there is a correlation between the formation of active -OOH species and the activity, which we link to the surface morphology of the anodes. The conventional approach to determine the electrochemical active surface area (ECSA) of metal-oxide electrodes is based on the analysis of the capacitive current during CV cycling.[41] Our attempts to utilize this approach showed that within the standard deviations of the determined double layer capacitance, no significant trend for our anodes could be observed. We thus assume that the method cannot be reliably applied to our electrode material. The respective data and discussion are given in the Section S6 (Supporting Information).

To correlate the structural analysis to the observed electrochemical performance, the contact angle measurements were correlated to the electrochemical activity after 8 h OER using 2D-kernel plots. Figure 9c shows that a decrease in contact angle corresponds to lower electrochemical activity, regardless of the solvent composition used in the ink formulation. A similar trend is observed between activity and surface roughness, as shown in Figure S8a (Supporting Information), as well as for the activity and PC correlation (Figure S8c, Supporting Information).

The close alignment of activity trends with surface roughness, PC, and contact angle suggests that the contact angle is strongly influenced by both surface roughness and PC. This observation further supports the Cassie-Baxter model of wetting behavior discussed in Section 2.3.1.

A higher lyophilicity commonly is expected to improve the accessibility of the electrolyte to the electrode surface, and hence more accessible active sites.[42] However, the presence of oxygen bubbles creates a complex three-phase contact line during OER. Studies on bubble detachment indicated that an increase in lyophobicity, i.e., lower lyophilicity, has a direct impact on gas adhesion. Surfaces with higher lyophobicity increase the gas bubble size and facilitate the removal of gas bubbles from the surface.[43,44] Specifically, Chang et al.[44] demonstrated that superhydrophobic surfaces facilitate the merging of small gas bubbles into larger ones, which detach more easily due to buoyancy. The non-wetted surface creates pathways for gas flow between adherend bubbles. The spontaneous growth of larger bubbles occurs as smaller ones combine, driven by capillary pressure differences.

Based on the above-mentioned studies, we assume that the super-lyophobic anode layers, W-50C and WE-50C, exhibit non-wetted regions that facilitate the movement and coalescence of smaller bubbles into larger ones. These larger bubbles can easily detach from the surface, preventing blockage and ensuring better access to the active sites. However, the static contact angle measurements serve only as a starting point for understanding this intricate transport phenomenon at the three-phase contact line. This behavior is not fully decoupled from dynamic contact angles under realistic conditions. We also have conducted potentiostatic electrochemical impedance spectroscopy (PEIS) measurements but found no possibility of quantifying this effect via the PEIS data, due to the complexity of the two-phase transport dynamics at the anode surface. The R_{ti} values shown do not provide information about the bubble transport at the anodes but instead reflect the influence of bubbles sticking on the surface on the change in ohmic resistance. The next step in this field would involve measuring dynamic contact angles and, ideally, monitoring the anode surface during bubble formation and detachment.

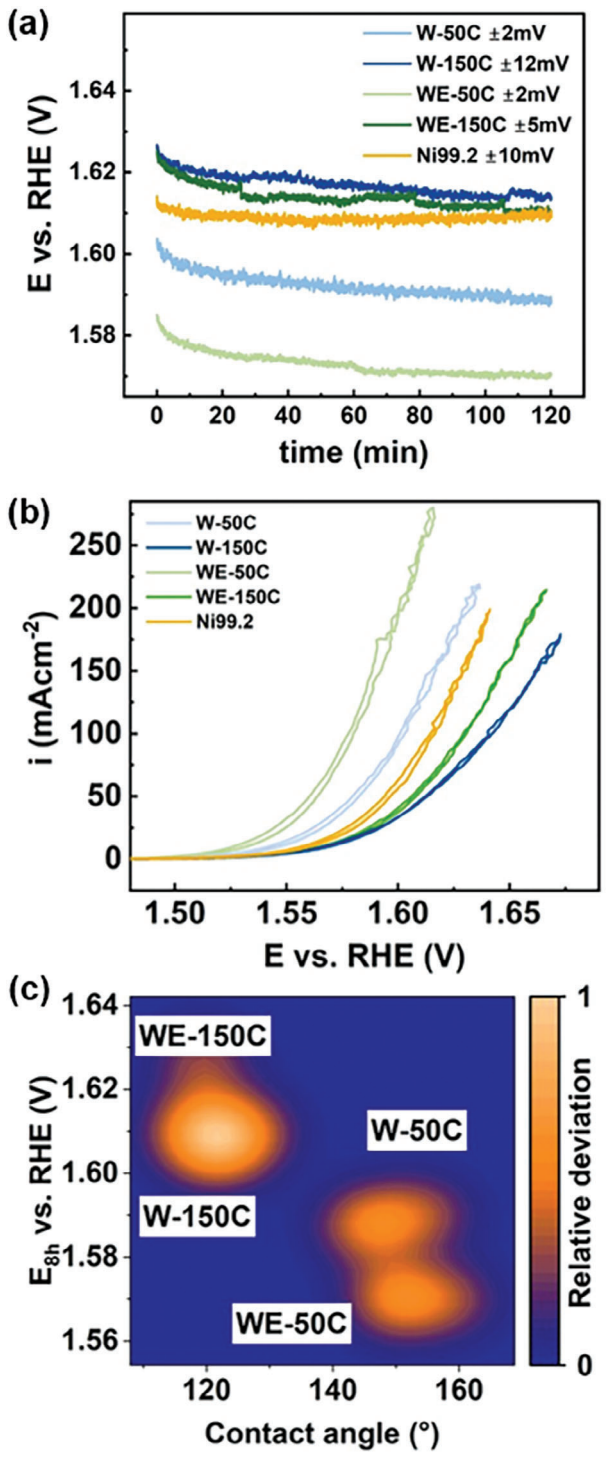

Figure 9. a) Short term stability (CP at 100 mA cm^{-2}) and b) dynamic activity (CV from 1 to 1.8 V, 5 mV s^{-1}) of the last protocol cycle c) kernel plots to correlate the potentials at 100 mA cm^{-2} after 4 × 2 h of stability measurements to the contact angles. For stability and activity measurements, three measurements were conducted (n = 3), while the results of the stability are represented as mean values with the averaged deviation indicated as SD in the legend. For the activity measurement, representative anodes were selected to illustrate the differences. Data on the two other measurements can be extracted from the Section S5 (Supporting Information).

Additionally, knowledge of microstructure and wetting properties provides a strong foundation for fluid dynamics studies, enabling comparisons between numerical results and detailed experimental data.

In our case, the anodes fabricated at 50 °C exhibit higher lyophobicity, according to the previously described factors, which can effectively improve bubble transport. This prevents blockage of active sites and ensures continuous exposure to the electrolyte. On the other hand, the high surface roughness in total exhibits more active sites, as was explained in the discussion of the conditioning of the anodes in section 2.4.3. Among the super-lyophobic layers, the electrochemical activity is slightly lower for W-50C compared to WE-50C. This difference might be attributed to the interparticle connectivity within the layers as described in section 2.3.2. Suvakov et al.[45] found in their study on modeling collective charge transport in nanoparticle assemblies, that weak nanoparticle network hinders electron transport by increasing resistance and introducing nonlinear current-voltage behavior due to fragmented conduction paths and structural inhomogeneities. In contrast, strong connectivity fosters continuous conductive pathways, enabling efficient charge transport with smoother current-voltage characteristics. Based on this study, we can speculate that stronger interparticle connectivity within the layers also enhances electron conductivity. Additionally, for constant operation electrolysis, the mechanical stability against delamination is likely improved by increased cohesion, thus also improving the durability of the anodes.

To sum up, in this study we fabricated four anode layers (W-50C, W-150C, WE-50C, and WE-150C) with constant composition but differing microstructure and macroscopic properties. These layers showed clear differences in electrocatalytic activity. The WE-50C layer outperformed the other layers and was produced based on a highly stable ink. The best-performing anode layers exhibited a hill-like surface morphology with increased surface roughness causing beneficial lyophobicity. Additionally, this layer exhibited a binder-mediated improved mechanical strength that resulted in a reduced R_u. Deciphering the effects of solvent composition and drying temperature on anode properties such as wetting and mechanical strength required extensive experimental and analytical work. These efforts underscored the inherent complexity of the interdependent microstructure, wetting, mechanical cohesion, and electrochemical performance. While this study provides valuable insights into their individual effects, exploring the intricate interactions between these two factors and other processing parameters presents an exciting and important avenue for future research. However, as a first step, in this work, we were able to showcase that altogether these parameters increased the electrochemical performance and how they enable a rational, knowledge-based electrode development in the future, where electrochemical target properties can be maximized by tailoring the wetting and adhesion properties via the microstructure (**Figure 10**).

3. Conclusion

In conclusion, we demonstrated the effect of anode layer microstructure as a proof-of-principle for achieving efficient OER. For this investigation, we employed two different solvent compositions and two distinct drying temperatures. Subsequently, the

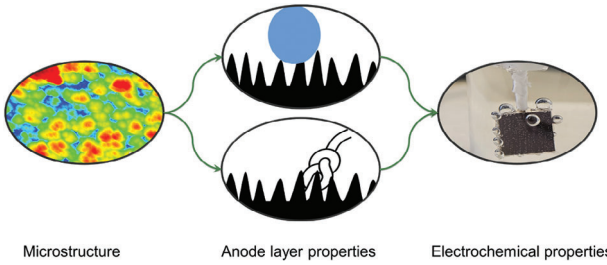

Figure 10. Strategic approach for maximizing the performance of the anode layers by optimizing their macroscopic properties via the microstructure.

microstructure and macroscopic properties of the anodes were identified and quantified. These properties are correlated to electrocatalytic activity and stability.

We found that the solvent composition has a more significant impact on the stability of catalyst inks and the mechanical strength of the anode layers, while the drying temperature predominantly influences surface features and wettability. At 50 °C, slower evaporation leads to the formation of islands and a highly porous microstructure, along with increased surface roughness, thereby enhancing lyophobicity. Conversely, at 150 °C, rapid evaporation results in the formation of concave, hemisphere-shaped structures with lower PC and reduced surface roughness, leading to decreased lyophobicity. Anode layers with increased microstructure-mediated lyophobicity exhibited enhanced electrochemical performance by increasing the amount of available active sites and facilitating effective bubble transport. Moreover, at lower drying temperatures, the resulting higher mechanical adherence, characterized by stronger particle connectivity, reduced the R_u within the beaker cell.

Taken together, our study revealed that by optimizing the anode layer of a given material via its microstructure towards the unravelled wetting and adhesion properties, we can effectively transport bubbles, expose more active sites and reduce contact resistance. While the testing of our anodes at realistic conditions (flow cell, elevated temperature and electrolyte concentration) is beyond the scope of this work, our findings emphasize the importance of optimizing process parameters for thin-layer catalyst fabrication. These adjustments are pivotal parameters that must be carefully considered in the design and development of highly active and stable engineered anode layers for AWE using nano-sized metal oxides.

4. Experimental Section

Ink Preparation: Commercial Ni-Co-O nanoparticles (Co_2NiO, ≥99.9999%, CAS: 58591-45-0) were sourced from Sigma–Aldrich. Deionized (DI) water, with a resistance exceeding 18.1 MΩ, was obtained from a Milli-Q system. Nafion perfluorosulfonic acid (PFSA) 5% dispersion (D521) was acquired from Ion Power GmbH and integrated into the ink formulation without further modification. Two formulations were prepared: one using pure Milli-Q water and the other a mixture of Milli-Q water and analytical grade isopropanol as carrier liquids. The binder-to-catalyst ratio was maintained at 0.2, and the total solid concentration was set to 1 mg ml^{-1}. Initially, the catalyst was mixed with the selected carrier liquids. A tip Sonicator (Branson SFX550) dispersed the components for 12 min at an amplitude of 20%, operating in pulse mode with 1 s intervals of sonication and rest. Subsequently, Nafion was added, and the mixture was further sonicated for 6 min under the same conditions. An ice bath was employed to prevent the ink from overheating and re-agglomeration. Sonotrode heating characteristics were added in Figure S1c (Supporting Information).

Ink Characterization: All inks were characterized by utilizing analytical centrifugation (Analytical Centrifuge LUMisizer 6514–44, LUM GmbH). Samples of 410 µL were filled into polycarbonate (PC) tubes and placed inside the centrifuge. All measurements were conducted at 2500 RPM and 20 °C. The captured fingerprints were then converted into transmittograms for improved understanding and comparison.

Layer Fabrication: The inks were deposited onto Ni plates (99.2%, HMW Hauner, 1 cm^2 projected area) using an ultrasonic spray coater (Sono-Tek Co., NY). Prior to coating, the Ni plates were cleaned through a chemical etching process in a 1 M HCl solution for 5 min, followed by rinsing with acetone and then isopropanol, each for 5 min, in a sonication bath (Elmasonic S 30 H, Germany) at ambient temperature. The inks were applied at a constant flow rate of 0.4 ml min^{-1}, with a total of 80 layers being deposited. For uniform coating, the initial layer was sprayed horizontally across the plate. Subsequently, the spray direction was adjusted by 90 degrees, and the next layer was applied perpendicularly to the previous one. This alternating pattern continued until all 80 layers were completed. The final mass loading was assessed using a precision balance by using the A&D BM-22 microbalance, with the coatings achieving the loadings of ≈415 ± 34 µg cm^{-2}.

Layer Characterization: Morphological analysis was conducted using SAM-EDX with a Scanning Auger Nanoprobe 710 of the company Ulvac-Phi, equipped with an EDAX Octane Elite detector for EDX analysis. Surface topography measurements were obtained through AFM (TOSCA 400, Anton Paar Germany GmbH) using in-house-developed MSDQ. The methodologies and conditions applied in this study were consistent with those detailed in our previous work[22] and parameters utilized were summarized in supporting information, section S3.

For determination of PC, the anode layer on Ni plate was mounted on a SEM sample holder using copper tape. A Helios NanoLab 600i SEM with a focused ion beam (FIB) was employed for cross-section imaging. A protective platinum line (15 µm x 0.5 µm, 0.5 µm thick) was deposited to shield the structure from high-energy FIBs. A rectangular area (15 µm x 15 µm) adjacent to the platinum line was selected, and a 5 µm deep hole was created using a 6.5 nA FIB beam current. The undamaged wall beneath the platinum deposition was polished with lower current ion beams (up to 93 pA) to obtain a smooth cross-section. Finally, images at various resolutions were captured using the SEM. The images obtained from the FIB-SEM device were processed using a MATLAB R2022a algorithm. The algorithm enhances image contrast to distinguish catalyst particles from pores, then binarizes the images into black (catalyst) and white (pores) pixels. Porosity was calculated by determining the ratio of white pixels (pore area) to the total pixels, representing the PC of the anode layer.

To quantify the adherence and coherence of the coatings under tensile stress, the centrifugal adhesion analyzer LUMiFrac from the company LUM had been employed. For this method, the samples have to be prepared appropriately. First, the catalyst coated Ni substrate was glued to a stainless steel backplate and on the top of the anode layer a copper test mass with a round adapter of 10 mm diameter is placed using an acrylic adhesive tape with a PET backbone (Lohmann DuploCOLL 362.2). Thus, the sample was in between the backplate and the test mass. In the second step, the specimen was placed in tight clamps for 24 h at room temperature to ensure that the pressure sensitive adhesive was at its peak strength. Finally, the specimen was inserted into an aluminum guiding sleeve, such that the copper test mass is always at a 90° angle to the backplate and the Ni substrate. This assembly was placed into a detector on a centrifugal plate. The detector identified the frequency of rotation, at which the copper test mass breaks off from the coating. From this, the adherence had been calculated.

Contact Angle Measurements were performed using OCA15PRO equipment (Data Physics Instruments GmbH). The measurements were conducted with 1 M KOH as the liquid which was dropped at a drop-eject-rate of 5 µL s^{-1}.

XPS measurements were performed on two Ni-Co-O films (WE-50C, and WE-150C). Measurements were carried out using a near ambient pressure XPS equipped with an Al-Kα source that produces monochromated X-rays of energy 1486.6 eV. After recording the survey scans using a pass energy of 100 eV, high resolution scans of all desired elements such as Ni, Co, O, C, and F were recorded applying a pass energy of 20 eV and a resolution of 0.05 eV. Data analysis was performed using the CasaXPS software.

Raman analysis was conducted on all Ni-Co-O films using a DXR Raman microscope from Thermo Scientific. An excitation line of 532 nm, and laser power of 1 mW was employed to collect the spectra.

The powder X-ray diffraction patterns of the Ni-Co-O films were recorded using a Bruker D2 Phaser 2nd Generation in Bragg-Brentano geometry with Cu-Kα radiation ($\lambda = 1.54$ Å). A 0.6 mm divergency slit and a Lynxeye detector were used for the measurements.

Post-mortem SEM-EDX analysis was performed using a Hitachi Tabletop TM3030 scanning electron microscope, equipped with a Quantax70 detector for energy-dispersive X-ray spectroscopy. All samples were measured with a 15 kV accelerating voltage in the large current mode.

For EDX-analysis, three arbitrary points on each sample were measured. All data was given in normalized weight percent, whereas elements known to be introduced due to the electrochemical measurement procedure, i.e., potassium, were excluded from the datasets.

FTIR analysis was conducted to investigate the functional groups and chemical bonding in the anode coatings. FTIR spectra were recorded using FTIR spectrometer (Bruker, Vertex 80). The instrument was equipped with an RT-DLaTGS (Room Temperature Deuterated L-Alanine doped TriGlycine Sulphate) detector and a KBr beam splitter. The transmittance spectra were collected in the range of 4000—200 cm^{-1} with a resolution of 4 cm^{-1}. The measurements were conducted at room temperature under nitrogen atmosphere to prevent any contamination from moisture and CO_2 interference. Each spectrum was obtained by averaging 32 scans on three different spots for each sample to improve the signal-to-noise ratio and reproducibility. The obtained spectra were then subjected to baseline correction using Bruker OPUS to enhance the clarity and accuracy of the peaks.

Electrochemical Characterization: The fabricated layers were employed as working electrodes (WE) in a three-electrode beaker cell setup. The setup was a modified version of the cell presented by Thissen et al., also making it applicable for plate electrodes.[35] For this, a Ni rod (99.5 % trace metal base, HMW Hauner) with a 1 mm groove was employed as a current collector for the WEs. Mercury/mercury oxide (Hg/HgO, ALS Japan) and a fine mesh (De Nora) were employed as reference and counter electrodes, respectively. The former's potential was regularly tracked versus a true RHE.[46] 200 ml of 1 M KOH (TH Geyer) was employed as electrolyte, whereas iron (diluted in HNO3, Agilent) was added to reach a controlled concentration of 200 ppb for every batch. No stirring was applied during the measurements.

Gamry Interfaces 1010E and Ref3000 were employed as potentiostats/galvanostats equipped with Gamry Framework Data Acquisition Software Version 7 for controlling the electrochemical measurements. The same electrochemical protocol was employed for every sample, consisting of eight main steps that will be briefly discussed here. A detailed description of the protocol is found in the section S4 (Supporting Information).

The protocol starts with the conditioning of the electrodes by cycling the potential 50 times from 0.25-1.5 V versus RHE. This step was followed by determining the ECSA, by applying rapid CV cycling with increasing scan rates (5, 10, 25, 50, 100, 200, 400, and 800 mV s^{-1}, 5 cycles each). To assess the activity and stability change of the samples, four repetitions of the following three protocol steps were applied. First, the dynamic activity of the samples was measured by cycling the potential between 1–1.8 V versus RHE three times ("Activity") followed by stationary polarization (SP) of the electrodes. For the SP, the current was measured for 180 s at consecutive potentials of 1, 1.1, 1.2, 1.3, 1.4, 1.45, 1.5, 1.55, 1.6, 1.65, 1.7, 1.75, and 1.8 V versus RHE. The final step in the cycles consisted of a 2 h CP measurement at 100 mA cm^{-2} ("Stability"). After the final cycle, the ECSA was determined with the same procedure as explained above. Before every protocol step, the R_u was determined via PEIS at open circuit potential (AC voltage 10 mV rms, 300 000 Hz–1000 Hz, 10 points per decade). The R_u was determined at the lowest absolute difference from the PEIS-phase from zero. All protocol steps were corrected with 100% of their respective R_u value.

Statistical Analysis: Initially, inks were prepared twice and characterized twice. The data was processed and was presented as mean ± SD. These two sets of inks, prepared under identical conditions, were coated onto Ni plates, resulting in 20 electrodes for each ink, for a total of 40 anodes. Microstructure analyses were conducted on individual anodes, with consideration given to the time required for the measurements. A multistage data quantification approach was employed for surface feature extraction, ensuring the provision of representative data across the anode surface. Anode layer properties (wetting and mechanical strength) were conducted with at least three measurements each to ensure the shown data were representative and reproducible. The results were presented as mean ± SD or range, either in tables within each section or in the accompanying figures. For electrochemical stability measurements, the plotted data represents the mean values obtained from three anodes, with the displayed SD calculated as the average SD at each time point. For the plotted CV data of activity and conditioning measurements, a representative set of anodes to effectively demonstrate the findings was selected. They do not include mean and SD values, as the potential values were corrected for R_u after the measurements. This correction introduces deviations in both the abscissa and ordinate, prohibiting averaging. However, the full data set was included in Section S5 (Supporting Information). Statistical analysis was performed using MATLAB R2022a and OriginPro 2024. All the data is openly available on the centralized data management platform.[47]

Supporting Information

Supporting Information is available from the Wiley Online Library or from the author.

Acknowledgements

A.J. and C.M. contributed equally to this work and share first authorship. A.J. appreciates the International Max Planck Research School (IMPRS) Recharge graduation school for support. Michael Poschmann and Marius Podleska were acknowledged for their help with the XRD measurements. Authors acknowledge the financial support from the Federal Ministry of Education and Research (PrometH2eus project in the framework of H_2Giga, funding numbers were 03HY105F and 03HY105A). D.S. is thankful for support by the Mercator Research Center Ruhr (MERCUR.Exzellenz, "DIMENSION" Ex-2021-0034), L.G. thanks Deutsche Forschungsgemeinschaft (DFG, German Research Foundation) – IRTG 2803 – 461605777 for the financial support, VV thanks university of Duisburg-Essen for Postdoc Seed Funding.

Open access funding enabled and organized by Projekt DEAL.

Conflict of Interest

The authors declare no conflict of interest.

Data Availability Statement

The data that support the findings of this study are openly available in Zenodo.[47]

Keywords

alkaline water electrolysis, Cassie-Baxter model, catalyst layer, drying process, morphology, oxygen evolution reaction, ultrasonic spray coating

Received: November 5, 2024
Revised: December 10, 2024
Published online: January 9, 2025

[1] H. Ikeda, R. Misumi, Y. Nishiki, Y. Kuroda, S. Mitsushima, *Electrochim. Acta* **2023**, *452*, 142283.
[2] K. Torii, M. Kodama, S. Hirai, *Int. J. Hydrogen Energy* **2021**, *46*, 35088.
[3] a) D. Segets, U.-P. Apfel, *ChemCatChem* **2024**, *16*, 202400678; b) D. Siegmund, S. Metz, V. Peinecke, T. E. Warner, C. Cremers, A. Grevé, T. Smolinka, D. Segets, U.-P. Apfel, *JACS Au* **2021**, *1*, 527.
[4] T. ul Haq, Y. Haik, *Appl. Catal., B* **2023**, *334*, 122853.
[5] a) D. Navas, S. Fuentes, A. Castro-Alvarez, E. Chavez-Angel, *Gels* **2021**, *7*, 275; b) A. P. LaGrow, M. O. Besenhard, A. Hodzic, A. Sergides, L. K. Bogart, A. Gavriilidis, N. T. K. Thanh, *Nanoscale* **2019**, *11*, 6620; c) Z. Xing, Z. Ju, J. Yang, H. Xu, Y. Qian, *Nano Res.* **2012**, *5*, 477; d) J. Wang, Y. Zhu, X. Zhong, Z. Hu, W.-H. Huang, C.-W. Pao, H. Cheng, N. Alonso-Vante, J. Ma, *Energy Adv.* **2024**, *3*, 2002; e) S. Angel, F. Schneider, S. Apazeller, W. Kaziur-Cegla, T. C. Schmidt, C. Schulz, H. Wiggers, *Proc. Combust. Inst.* **2021**, *38*, 1279; f) S. Angel, J. D. Tapia, J. Gallego, U. Hagemann, H. Wiggers, *Energy Fuels* **2021**, *35*, 4367; g) S. Angel, J. Neises, M. Dreyer, K. Friedel Ortega, M. Behrens, Y. Wang, H. Arandiyan, C. Schulz, H. Wiggers, *AIChE J.* **2020**, *66*, 441; h) L. Carvajal, R. Buitrago-Sierra, A. Santamaría, S. Angel, H. Wiggers, J. Gallego, *J. Therm. Spray Tech.* **2020**, *29*, 368.
[6] a) X. G. Jiang, Y. P. Zhang, C. Song, Y. C. Xie, T. K. Liu, C. M. Deng, N. N. Zhang, *Int. J. Hydrogen Energy* **2020**, *45*, 33007; b) S. Storbakken, *Fabrication and Testing of Inkjet Printed Electrodes for Anion Exchange Membrane Water Electrolysis*, University of Alberta Library, **2022**, https://era.library.ualberta.ca/items/d1db0fd4-6dff-4738-a436-5c2f1dc5fdad.
[7] D. Segets, C. Lutz, K. Yamamoto, S. Komada, S. Süß, Y. Mori, W. Peukert, *J. Phys. Chem. C* **2015**, *119*, 4009.
[8] M. Grzelczak, J. Vermant, E. M. Furst, L. M. Liz-Marzán, *ACS Nano* **2010**, *4*, 3591.
[9] a) P.-E. Delannoy, B. Riou, T. Brousse, J. L. Bideau, D. Guyomard, B. Lestriez, *J. Power Sources* **2015**, *287*, 261; b) S. Shetty, M. M. Jaffer Sadiq, D. K. Bhat, A. C. Hegde, *J. Electroanal. Chem.* **2017**, *796*, 57; c) N. H. Faisal, A. Prathuru, R. Ahmed, V. Rajendran, M. Hossain, V. Venkatachalapathy, N. K. Katiyar, J. Li, Y. Liu, Q. Cai, B. A. Horri, D. Thanganadar, G. Singh Sodhi, K. Patchigolla, C. Fernandez, S. Joshi, S. Govindarajan, V. Kurushina, S. Katikaneni, S. Goel, *ChemNanoMat* **2022**, *8*, 202200384.
[10] a) Y. Deo, N. Thissen, A. K. Mechler, *Meet. Abstr.* **2023**, *MA2023-02*, 1255; b) S. M. Al-Zuraiji, T. Benkó, K. Frey, Z. Kerner, J. S. Pap, *Catalysts* **2021**, *11*, 577; c) Z. Yan, H. Liu, Z. Hao, M. Yu, X. Chen, J. Chen, *Chem. Sci.* **2020**, *11*, 10614.
[11] a) T.-H. Huang, H.-L. Shen, T.-C. Jao, F.-B. Weng, A. Su, *Int. J. Hydrogen Energy* **2012**, *37*, 13872; b) B. Millington, V. Whipple, B. G. Pollet, *J. Power Sources* **2011**, *196*, 8500; c) T. Jaster, S. Albers, A. Leonhard, M.-A. Kräenbring, H. Lohmann, B. Zeidler-Fandrich, F. Özcan, D. Segets, U.-P. Apfel, *J. Phys. Energy* **2023**, *5*, 024001.
[12] a) Y. Z. N. Htwe, M. Mariatti, J. Khan, *J. Mater. Sci.: Mater. Electron.* **2024**, *35*, 1191; b) M. Braun, M. Chatwani, P. Kumar, Y. Hao, I. Sanjuán, A.-A. Apostoleri, A. C. Brix, D. M. Morales, U. Hagemann, M. Heidelmann, *J. Phys. Energy* **2023**, *5*, 024005.
[13] S. Bapat, D. Segets, *ACS Appl. Nano Mater.* **2020**, *3*, 7384.
[14] M.-A. Kräenbring, L. Wickert, M. Hansen, S. Sanden, K. Pellumbi, J. Wolf, D. Siegmund, F. Özcan, U.-P. Apfel, D. Segets, *ChemCatChem* **2024**, *16*, 202301273.
[15] L. Zolin in, *PoliTO Springer Series*, (Ed.: L. Zolin), Springer International Publishing, Cham, **2017**, pp. 77–94.
[16] D. Chanda, J. Hnát, T. Bystron, M. Paidar, K. Bouzek, *J. Power Sources* **2017**, *347*, 247.
[17] H.-Y. Jung, J. W. Kim, *Int. J. Hydrogen Energy* **2012**, *37*, 12580.
[18] a) J. Benziger, A. Bocarsly, M. J. Cheah, P. Majsztrik, B. Satterfield, Q. Zhao in *Structure and Bonding*, (Eds.: A. Bocarsly, D. M. P. Mingos), Springer Berlin Heidelberg, Berlin, Heidelberg, **2011**, 85; b) T. Agarwal, A. K. Prasad, S. G. Advani, S. K. Babu, R. L. Borup, *J. Mater. Chem. A* **2024**, *12*, 14229.
[19] J. Mališ, P. Mazúr, M. Paidar, T. Bystron, K. Bouzek, *Int. J. Hydrogen Energy* **2016**, *41*, 2177.
[20] S. Süß, T. Sobisch, W. Peukert, D. Lerche, D. Segets, *Adv. Powder Technol.* **2018**, *29*, 1550.
[21] a) I. S. Khattab, F. Bandarkar, M. A. A. Fakhree, A. Jouyban, *Korean J. Chem. Eng.* **2012**, *29*, 812; b) K. H. Musa, A. Abdullah, K. Jusoh, V. Subramaniam, *Food Anal. Methods* **2011**, *4*, 100.
[22] A. Jain, V. Vinayakumar, A. Olean-Oliveira, C. Marcks, M. Chatwani, A. K. Mechler, C. Andronescu, D. Segets, *ChemCatChem* **2024**, *16*, 202301461.
[23] B. Sobac, D. Brutin, *Phys. Rev. E* **2012**, *86*, 21602.
[24] C. Aberle, M. Lewis, G. Yu, N. Lei, J. Xu, *Soft Matter* **2011**, *7*, 11314.
[25] a) R. Chen, L. Zhang, D. Zang, W. Shen, in *Wetting and Drying of Colloidal Droplets. Physics and Pattern Formation*, (Ed.: R. Chen), IntechOpen, **2016**, https://www.intechopen.com/chapters/52575; b) H. Yoo, C. Kim, *Colloids Surf. A* **2015**, *468*, 234; c) S. Erkan, in *Progress in Clean Energy*, (Eds.: I. Dincer, C. O. Colpan, O. Kizilkan, M. A. Ezan), Springer International Publishing, Cham, **2015**, *2*, 481.
[26] a) Y. Yoon, D. Kim, J.-B. Lee, *Micro and Nano Syst Lett* **2014**, *2*, 3; b) B. Wang, W. Liang, Z. Guo, W. Liu, *Chem. Soc. Rev.* **2015**, *44*, 336.
[27] S. Węglarczyk, *ITM Web Conf.* **2018**, *23*, 00037.
[28] a) W. Jiang, J. Li, C. Zhao, W. Cheng, J. Liu, Y. Chen, *Int. J. Hydrogen Energy* **2024**, *51*, 1486; b) T. Koishi, K. Yasuoka, S. Fujikawa, T. Ebisuzaki, X. C. Zeng, *Proc. Natl. Acad. Sci. USA* **2009**, *106*, 8435.
[29] a) W. Xu, Z. Lu, X. Sun, L. Jiang, X. Duan, *Acc. Chem. Res.* **2018**, *51*, 1590; b) J. Das, S. Mandal, A. Borbora, S. Rani, M. Tenjimbayashi, U. Manna, *Adv. Funct. Mater.* **2024**, *34*, 2311648; c) A. Forner-Cuenca, V. Manzi-Orezzoli, J. Biesdorf, M. E. Kazzi, D. Streich, L. Gubler, T. J. Schmidt, P. Boillat, *J. Electrochem. Soc.* **2016**, *163*, F788.
[30] L. Chaabane, L. Dammak, D. Grande, C. Larchet, P. Huguet, S. V. Nikonenko, V. V. Nikonenko, *J. Membr. Sci.* **2011**, *377*, 54.
[31] M. Mekala, B. Neerudi, P. R. Are, R. Surakasi, G. Manikandan, V. R. Kakara, A. A. Dhumal, *Adsorpt. Sci. Technol.* **2022**, *2022*.
[32] P. Quarz, N. Zimmerer, P. Scharfer, W. Schabel, *Fuel Cells* **2024**, *24*, 108.
[33] Z. Zhang, C. Gu, K. Wang, H. Yu, J. Qiu, S. Wang, L. Wang, D. Yan, *Catalysts* **2024**, *14*, 254.
[34] X. Xie, L. Du, L. Yan, S. Park, Y. Qiu, J. Sokolowski, W. Wang, Y. Shao, *Adv Funct Materials* **2022**, *32*, 2110036.
[35] N. Thissen, J. Hoffmann, S. Tigges, D. A. M. Vogel, J. J. Thoede, S. Khan, N. Schmitt, S. Heumann, B. J. M. Etzold, A. K. Mechler, *ChemElectroChem* **2024**, *11*, 202300432.
[36] C. Gohlke, J. Gallenberger, N. Niederprüm, H. Ingendae, J. Kautz, J. P. Hofmann, A. K. Mechler, *ChemElectroChem* **2024**, *11*, 202400318.
[37] a) F. Dionigi, Z. Zeng, I. Sinev, T. Merzdorf, S. Deshpande, M. B. Lopez, S. Kunze, I. Zegkinoglou, H. Sarodnik, D. Fan, *Nat. Commun.* **2020**, *11*, 2522; b) M. E. G. Lyons, R. L. Doyle, I. Godwin, M. O'Brien, L. Russell, *J. Electrochem. Soc.* **2012**, *159*, H932.
[38] Z. Chen, L. Cai, X. Yang, C. Kronawitter, L. Guo, S. Shen, B. E. Koel, *ACS Catal.* **2018**, *8*, 1238.
[39] V. Vinayakumar, T. Wagner, C. Marcks, J. Johny, G. Wartner, M. F. Tesch, I. Spanos, A. Ghafari, A. Jain, O. Prymak, Engineering Engrxiv Archive, **2024**.
[40] D. Y. Chung, P. P. Lopes, P. Farinazzo Bergamo Dias Martins, H. He, T. Kawaguchi, P. Zapol, H. You, D. Tripkovic, D. Strmcnik, Y. Zhu, *Nat. Energy* **2020**, *5*, 222.

[41] M. Schalenbach, V. Selmert, A. Kretzschmar, L. Raijmakers, Y. E. Durmus, H. Tempel, R.-A. Eichel, *Phys. Chem. Chem. Phys.* **2024**, *26*, 14288.
[42] F. Tang, W. Cheng, Y. Huang, H. Su, T. Yao, Q. Liu, J. Liu, F. Hu, Y. Jiang, Z. Sun, *ACS Appl. Mater. Interfaces* **2017**, *9*, 26867.
[43] R. Xu, D. Zhu, K. Du, D. Cui, H. Feng, W. Hao, D. Tian, Y. Du, *Mater. Today Energy* **2022**, *25*, 100961.
[44] F.-M. Chang, Y.-J. Sheng, S.-L. Cheng, H.-K. Tsao, *Appl. Phys. Lett.* **2008**, *92*, 264102.
[45] M. Suvakov, B. Tadić, *J. Phys. Condens. Matter* **2010**, *22*, 163201.
[46] G. Jerkiewicz, *ACS Catal.* **2020**, *10*, 8409.
[47] A. Jain, C. Marcks, L. Grebener, J. Johny, A. S. Ahammed, M. Chatwani, M.-A. Kräenbring, A. Shaji, M. F. Tesch, A. K. Mechler, V. Vinayakumar, D. Segets, *Zenodo* **2024**, https://doi.org/10.5281/ZENODO.14554548.